Received: 8 December 2021 | Accepted: 8 August 2022

DOI: 10.1111/1365-2478.13265

Geophysical Prospecting | EAGE EUROPEAN ASSOCIATION OF GEOSCIENTISTS & ENGINEERS

ORIGINAL ARTICLE

A comparison of the joint and independent inversions for magnetic and gravity data over kimberlites in Botswana

Saeed Vatankhah[1] | **Rosemary Anne Renaut**[2] | **Kevin Mickus**[3] | **Shuang Liu**[4] | **Kitso Matende**[5]

[1]Institute of Geophysics, University of Tehran, Tehran, Iran

[2]School of Mathematical and Statistical Sciences, Arizona State University, Tempe, Arizona, USA

[3]Department of Geography, Geology and Planning, Missouri State University, Springfield, Missouri, USA

[4]Hubei Subsurface Multi-scale Imaging Key Laboratory, Institute of Geophysics and Geomatics, China University of Geosciences, Wuhan, China

[5]Department of Geology, University of Botswana, Gaborone, Botswana

Correspondence
Saeed Vatankhah, Institute of Geophysics, University of Tehran, Tehran, Iran.
Email: svatan@ut.ac.ir

Abstract

Complementary independent and joint focusing inversion investigations are applied to the magnetic and gravity datasets for two kimberlite pipes, BK54 and BK55, in Botswana. The magnetic data are high resolution and, clearly, indicate two anomalies in the survey area. Independent inversion of this magnetic data provides a focused image of the subsurface with sharp boundaries for both pipes. The extensions of the pipes are close to those estimated by the available boreholes in the area. The spatial resolution of the gravity data is, on the other hand, relatively poor. The BK54 pipe does not appear on the residual gravity anomaly, while the BK55 is characterized by a positive anomaly. Independent inversion of the gravity data provides the geometry of the BK55 but does not identify the BK54 pipe. While there are some lower density materials in the place of the BK54 pipe, no specific target is revealed. Furthermore and relevant is that the reconstructed model for BK55 is not focused. A joint focusing inversion based on the structural cross-gradient linkage is applied for the combined gravity and magnetic datasets. This algorithm produces structurally similar magnetic susceptibility and density models. A lower density distribution of material, similar to that of the magnetic susceptibility distribution, is revealed for the BK54 pipe. Moreover, in contrast to the result obtained by an independent inversion, the structure for BK54 is connected at depth, and the reconstructed models of BK54 and BK55 share the sparsity. The models are not as sparse as the magnetic susceptibility model that is obtained independently, but they are more focused than the independently obtained density model. A comprehensive comparison of the reconstructed models, and also computational CPU time, for independent and joint inversions is presented.

KEYWORDS

Botswana, gravity, joint inversion, magnetic, sparsity

INTRODUCTION

Modern-day geophysical surveys provide a variety of different datasets, including, for example, gravity, seismic, magnetic and electromagnetic datasets that can be used for analysis of the geophysical subsurface structures. Computational analysis of the data aims to provide improved geophysical interpretation of the underlying process and structure and is used to extract important information from models that are not inherently unique. The use of combinations of datasets along with the imposition of constraints obtained using prior geological mapping and drill hole data is used to reduce the ambiguity in the interpretation. Inverse methods, either inverting a single dataset or jointly inverting multiple datasets, are commonly

 © 2022 European Association of Geoscientists & Engineers.

13652478, 2022, 9, Downloaded from https://onlinelibrary.wiley.com/doi/10.1111/1365-2478.13265 by Arizona State University Acq & Analysis, Lib Continuations, Wiley Online Library on [19/10/2022]. See the Terms and Conditions (https://onlinelibrary.wiley.com/terms-and-conditions) on Wiley Online Library for rules of use; OA articles are governed by the applicable Creative Commons License

used to estimate the physical and geometric parameters of the subsurface target(s) (Boulanger & Chouteau, 2001; Gallardo & Meju, 2004; Last & Kubik, 1983; Leliévre et al., 2012; Portniaguine & Zhdanov, 1999; Zhdanov et al., 2012). There are, in general, two main strategies to deal with the inversion of multiple datasets: (i) an independent inversion of each dataset can be performed to provide its related subsurface model. The independently obtained reconstructed models are considered and interpreted together in order to present a final model for the subsurface (Leliévre et al., 2012). (ii) A joint and simultaneous inversion of multiple datasets can be implemented. In this case, a direct or indirect linkage between the multiple model parameters is imposed (Leliévre et al., 2012), and the joint inversion restricts the models to only those that predict the observed datasets and satisfy the linkage constraint. There have been many successful applications of joint inversion of multiple geophysical datasets (Fregoso & Gallardo, 2009; Fregoso et al., 2015; Gallardo & Meju, 2003, 2004; Haber & Oldenburg, 1997; Haber & Holtzman Gazit, 2013; Lin & Zhdanov, 2018; Leliévre et al., 2012; Moorkamp et al., 2011; Nielsen & Jacobsen, 2000; Tryggvason & Linde, 2006; Zhdanov et al., 2012). In particular, when different datasets are sensitive to variations within specific sections of the subsurface target(s), a joint inversion process may be able to reduce, and sometimes significantly, the ambiguity of the reconstructed model. For example, ground magnetic and gravity data are both more sensitive to near-surface structures, while borehole gravity and magnetic data, or crosswell seismic tomography, can provide valuable information about deeper structures. Ideally, a joint inversion of surface and borehole data may increase the reliability of the reconstructed subsurface model (Leliévre et al., 2012). In some surveys, however, such datasets are not available. For example, in mineral exploration, it is common to only have surface or airborne gravity and magnetic data. On the other hand, in a number of cases, the spatial resolution of the datasets differs. Although the use of multiple datasets offers a potential for improved resolution of the underlying models by using a joint inversion process, the computational costs and memory requirements are far less when the datasets are inverted independently. Further, there are fewer challenges involved in determining the parameters that impact the solution of the inversion algorithm for a single inversion as compared that using a joint inversion. For example, for an individual inversion, we need to determine only one regularization parameter for each dataset inversion and several automated algorithms can be used to estimate this parameter. Because it is feasible to find the regularization parameter effectively and efficiently, the single inversion process converges quickly. On the other hand, for a joint inversion of two datasets, we need to estimate at least three weighting parameters, for which there are currently no automatic algorithms. Thus, it is necessary to apply heuristic approaches to identify the appropriate weighting parameters, and generally algorithms for joint inversion converge more slowly. It is, therefore, important to consider the trade-offs between improved interpretation and computational costs when discussing the efficiency of a joint inversion algorithm in contrast to the independent inversion. In this study, we present a comprehensive comparison of the application of the independent and joint inversions for gravity and magnetic data acquired over kimberlite pipes in north-central Botswana (Matende & Mickus, 2021).

Kimberlites are a type of potassic volcanic rock best known for sometimes containing diamonds. Magnetic, electromagnetic and gravity surveys are usually used for the exploration of kimberlites (LaFehr & Nabighian, 2012). Gravity and magnetic anomalies over kimberlites are quite variable and depend on the physical properties of the kimberlitic material, the lithologies the kimberlite intruded into and the degree of weathering of the kimberlitic material (Kamara, 1981; Kjarsgaard, 2007). Most magnetic anomalies are positive due to the presence of magnetic minerals within the kimberlite root (hypabyssal material) and the overlying diatreme material (Devriese et al., 2017; Kjarsgaard, 2007). However, the resultant gravity anomalies are more difficult to assess due to the weathering of the kimberlitic material, kimberlites being intruded into Proterozoic and Archean metamorphic rocks. Density measurements have shown that the density increases with depth from 2.4 to 3.0 g cm^{-3} through the pyroclastic material to the kimberlite root material (Power & Hildes, 2007). The presence of a thick low-density crater material at the surface commonly overwhelms the higher density material at depth to produce a negative gravity anomaly (Kamara, 1981; Kjarsgaard, 2007). Thus, a majority of published results have shown that there is a negative gravity anomaly over the kimberlite pipes due to a thick crater facies (Costa, 1989; Power & Hildes, 2007), lack of a density contrast between the dense kimberlite root and the surrounding lithologies (Devriese et al., 2017; Masun et al., 2004); and a combination of a thick crater material and weathering of the kimberlite root (Pettit, 2009). However, some kimberlites have been associated with no gravity anomalies (Pettit, 2009) and with positive gravity anomalies (Kamara, 1981; Kjarsgaard, 2007; Pettit, 2009). A positive gravity anomaly was observed over kimberlite in Angola, where the anomaly was explained by a magmatic plug at the centre of the pipe (Pettit, 2009). Additionally, small amplitude positive gravity anomalies (1–2 mGal) due to a large volume of unweathered kimberlite material were observed in Australia (Kamara, 1981).

In this study, we use ground gravity and magnetic data from the Orapa kimberlite field in north-central Botswana, which is a well-known diamond-producing region. The Orapa kimberlite field contains over 50 kimberlite pipes, and the well-known diamond-producing mines at Orapa are Damtshaa, Karowe and Letlhakane (Field & Scott Smith, 1999). Over the past three decades, geophysical exploration has

13652478, 2022, 9, Downloaded from https://onlinelibrary.wiley.com/doi/10.1111/1365-2478.13265 by Arizona State University Acq & Analysis, Lib Continuations, Wiley Online Library on [19/10/2022]. See the Terms and Conditions (https://onlinelibrary.wiley.com/terms-and-conditions) on Wiley Online Library for rules of use; OA articles are governed by the applicable Creative Commons License

discovered several smaller kimberlite pipes and two of these pipes, hereafter called BK54 and BK55, have been found from ground magnetic and gravity surveys. Subsequent drilling has also confirmed the presence of the kimberlite material (Matende & Mickus, 2021). A residual magnetic anomaly constructed by Matende and Mickus (2021), clearly, outlines both the BK54 and BK55 pipes. On the other hand, the BK54 pipe does not appear on the residual gravity anomaly map, while the BK55 pipe is characterized by a small amplitude positive gravity anomaly (Matende & Mickus, 2021). The BK54 pipe is associated with a small amplitude residual gravity minimum probably related to the crater material over the main kimberlite material. Matende and Mickus (2021) performed an integrated analysis of the gravity, magnetic and drillhole data by performing a map analysis (tilt derivatives, residual anomalies), three-dimensional (3D) inversion and two and one-half (2.5D) forward modelling, to determine the geometry, physical properties and formation of the pipes. Even though they did an integrated analysis, they only applied independent minimum structure inversions of the gravity and magnetic datasets. These inversions can only produce smooth models with blurred boundaries and do not permit the detection of sharp boundaries. In this study, we contrast the results that are obtained using both an independent focusing inversion algorithm, based on an L_1-norm of the model parameters, for each of the gravity and magnetic datasets, with the results obtained using a joint focusing inversion applied for both datasets together. The focusing inversion is chosen for its ability to provide compact models of the subsurface target(s) and here specifically to assist with defining the BK54 and BK55 pipes.

There have been several efficient algorithms developed for the inversion of gravity and magnetic data. These can generally be categorized into two main groups: (i) algorithms that produce smooth and simple models, with as little structure as possible, which normally use a stabilizer that employs an L_2-norm of the gradient of the model parameters (Constable et al., 1987; Li & Oldenburg, 1996; Pilkington, 1997) and (ii) algorithms that apply L_p-norm stabilizers, $0 \leq p < 2$, of the model parameters, or for a gradient of the model parameters, in order to produce sharp and focused, or *blocky*, models (Barbosa & Silva, 1994; Last & Kubik, 1983; Portniaguine & Zhdanov, 1999; Vatankhah et al., 2017; Zhdanov & Tolstaya, 2004). More recently, multiple combinations of these stabilizers have also been applied within the context of independent inversions of magnetic or gravity datasets (Fournier & Oldenburg, 2019; Sun & Li, 2014; Sun & Wei, 2021). On the other hand, Vatankhah et al. (2022) presented a general algorithm for the reconstruction of the smooth and/or sparse models for the joint inversion of gravity and magnetic datasets in which the cross-gradient constraint is imposed as a linkage between density and susceptibility models. In this way, the topology of the models is used during the joint inversion in order to enhance the structural similarity of the reconstructed models.

In the present study, we provide a short review of the independent and joint inversion algorithms used to investigate the kimberlite pipes in Botswana. A detailed discussion of the geology, gravity and magnetic datasets, and previous results for Orapa kimberlite pipes is provided. The Botswana gravity and magnetic datasets are inverted using both independent and joint inversion algorithms and contrasted with the prior inversion results from the literature.

INVERSION METHODOLOGY

To formulate the problem, we consider the standard strategy in which the subsurface is discretized into a set of rectangular prisms with fixed size but unknown physical properties. We suppose that $\mathbf{d}_i^{\text{obs}} \in \mathcal{R}^N$ indicates a set of N measurements, and $\mathbf{m}_i \in \mathcal{R}^M$ is the vector of M unknown model parameters ($N \ll M$), where $\mathbf{m}_1$ and $\mathbf{m}_2$ represent the magnetic susceptibility and density contrast, respectively. In general, we use index $i = 1$ and $i = 2$ to refer to variables associated with the magnetic and gravity problems, respectively. Further, we use $\mathbf{G}_i \in \mathcal{R}^{N\times M}$ as the discretization of the forward model operator that connects the data and related parameters

$$\mathbf{d}_i^{\text{obs}} = \mathbf{G}_i\mathbf{m}_i \quad i = 1, 2. \tag{1}$$

The aim is to determine a geologically plausible model $\mathbf{m}_i$ that predicts $\mathbf{d}_i^{\text{obs}}$ at the noise level.

It is well known that the inversion of potential field data is an ill-posed problem. As a consequence, to handle the inherent non-uniqueness of the problem, so as to find stable but plausible solutions, it is always necessary to impose regularization, or stabilization, as well as to constrain the parameters to geologically plausible values. For stabilization, we use the L_1-norm strategy, developed by Vatankhah et al. (2017), in which a global objective function, $\mathbf{P}_i^{\alpha_i}(\mathbf{m}_i)$, consisting of a data misfit function, $\mathbf{\Phi}(\mathbf{d}_i)$, and a stabilizing term, $\mathbf{\Psi}(\mathbf{m}_i)$, is constructed as

$$\begin{aligned}\mathbf{P}_i^{\alpha_i}(\mathbf{m}_i) &= \mathbf{\Phi}(\mathbf{d}_i) + \alpha_i^2\mathbf{\Psi}(\mathbf{m}_i)\\ &= \|\mathbf{W}_{\mathbf{d}_i}(\mathbf{G}_i\mathbf{m}_i - \mathbf{d}_i^{\text{obs}})\|_2^2 + \alpha_i^2\|(\mathbf{W}_{\text{depth}})_i(\mathbf{W}_{\text{h}})_i(\mathbf{W}_{\text{L}})_i(\mathbf{m}_i - \mathbf{m}_i^{\text{apr}})\|_2^2.\end{aligned} \tag{2}$$

Diagonal matrix $\mathbf{W}_{\mathbf{d}_i} = \text{diag}(1/\eta_{ji})$, $j = 1, \cdots, N$, provides weights dependent on the noise level in the data. Here, η_{ji} is the standard deviation of the noise in the jth datum, for the ith dataset. Scalar weights $\alpha_i > 0$ are the regularization parameters which balance the data misfit and stabilizing terms, and their determination is an important step in any regularization method. The initial models $\mathbf{m}_i^{\text{apr}} \in \mathcal{R}^M$, in combination

13652478, 2022, 9, Downloaded from https://onlinelibrary.wiley.com/doi/10.1111/1365-2478.13265 by Arizona State University Asu & Analysis, Lib Continuations, Wiley Online Library on [19/10/2022]. See the Terms and Conditions (https://onlinelibrary.wiley.com/terms-and-conditions) on Wiley Online Library for rules of use; OA articles are governed by the applicable Creative Commons License

with hard constraint matrices $(\mathbf{W}_\mathrm{h})_i \in \mathcal{R}^{M\times M}$, facilitate the inclusion of initial estimates for the models. If the physical properties of some prisms are known, these values may be included in $\mathbf{m}_i^{\mathrm{apr}}$ and the corresponding entries on the diagonals of the respective $(\mathbf{W}_\mathrm{h})_i$ are set to a large value. Consequently, known values are held during the inversion which only updates unknown model parameters within any iterative scheme. In the absence of such information, $\mathbf{m}_i^{\mathrm{apr}}$ and $(\mathbf{W}_\mathrm{h})_i$ are set to the zero vector and the identity matrix, respectively. In potential field inverse problems, the recovered models are usually concentrated near the surface, due to the decay of the kernels with depth. This is a direct consequence of the lack of a priori information. To allow the algorithm to generate models with structure at depth, Li and Oldenburg (1996) introduced a diagonal depth-weighting matrix $(\mathbf{W}_{\mathrm{depth}})_i \in \mathcal{R}^{M\times M}$. With the application of this matrix, now, all prisms have an approximately equal probability of contributing to the solution during the inversion process. Entries along the diagonal in $(\mathbf{W}_{\mathrm{depth}})_i$ that correspond to a prism with mean depth z_ℓ have the value $1/(z_\ell + z_a)^{\beta_i}$, where generally z_a is the average observation height above the surface for the measured data and β_i is model specific. Here we follow the formula given in Boulanger and Chouteau (2001), which uses the exponent β in the denominator, rather than $\beta/2$ as used by Li and Oldenburg (1996). For our experiments, we use $\beta_1 = 1.4$ and $\beta_2 = 0.8$, for the magnetic and gravity problems, respectively. With the $1/2$ scaling, these values are close to those suggested by Li and Oldenburg (1996) and, without the scaling, are within the ranges suggested by Boulanger and Chouteau (2001). On the other hand, Cella and Fedi (2012) presented an alternative flexible depth-weighting approach for potential field data inversion. In their approach, the depth-weighting function is associated with the field decay of the whole source and not with a single prism. Thus, the depth-weighting function is given with the structural indices of the different sources as the exponent (Cella & Fedi, 2012). Here we follow the strategy presented by Li and Oldenburg (1996) for depth weighting. Further, ambiguity in the inversion is reduced by imposing bound constraints for the solution given prior information, $\mathbf{m}_i^{\min}$ and $\mathbf{m}_i^{\max}$, for desired target structures. Then, $\mathbf{m}_i$ is given iteratively by

$$\mathbf{m}_i(\alpha_i) = \underset{\mathbf{m}_i^{\min}\le\mathbf{m}_i\le\mathbf{m}_i^{\max}}{\operatorname{argmin}} \{\mathbf{P}_i^{\alpha_i}(\mathbf{m}_i)\}, \tag{3}$$

where the nonlinearity of (3) arises in part because the diagonal weighting matrices $(\mathbf{W}_\mathrm{L})_i \in \mathcal{R}^{M\times M}$ are dependent on $\mathbf{m}_i$. They arise from the approximation of the original L_1-norm stabilizer with the L_2-norm term as shown in (2); see Vatankhah et al. (2017) for details. The entries are defined componentwise by $((\mathbf{m}_i - \mathbf{m}_i^{\mathrm{apr}})^2 + \varepsilon^2)^{-1/4}$, where $0 < \varepsilon \ll 1$ assures that $(\mathbf{W}_\mathrm{L})_i$ is non-singular. When $\varepsilon \ll 1$ solutions are generally sparse and compact, while larger values lead to smooth models. Here we use $\varepsilon^2 = 1e^{-9}$ in order to provide compact models with sharp boundaries. The solution is estimated using an iteratively reweighted least squares algorithm, as described in Vatankhah et al. (2017, Algorithm 1). To test the convergence of the solution at each iteration k, the $(\chi_i^2)^{(k)}$ value as given by

$$(\chi_i^2)^{(k)} = \|\mathbf{W}_{\mathbf{d}_i}(\mathbf{G}_i\mathbf{m}_i^{(k)} - \mathbf{d}_i^{\mathrm{obs}})\|_2^2, \quad i = 1, 2. \tag{4}$$

can be computed. The iteration terminates when $\frac{(\chi_i^2)^{(k)}}{N+\sqrt{2N}} \le 1$, Boulanger and Chouteau (2001), which means that the data produced by the candidate model should approximate the observed data at the noise level. Comprehensive details for the formulation given by (3), and related references, are presented in Vatankhah et al. (2020).

The strategy to solve (3) depends on the problem size. When the problem is of moderate size, it is possible to apply direct methods at each iteration, for example, the singular value decomposition (SVD) can be used to obtain the solution (Vatankhah et al., 2017). While this is not feasible for larger problems, it is still possible to apply iterative solvers or randomized algorithms that effectively yield solutions, which are dependent on an approximate SVD (Vatankhah et al., 2020).

Joint inversion

To invert the two datasets simultaneously, we apply the cross-gradient joint inversion algorithm, which was employed in Vatankhah et al. (2022). Suppose that here the block_stack $(\cdot,\cdot)$ is used to indicate the stacking of vectors with the same number of columns in one vector. Further, block_diag $(\mathbf{A},\mathbf{B})$ indicates a block diagonal matrix of size $(N_\mathbf{A} + N_\mathbf{B}) \times (M_\mathbf{A} + M_\mathbf{B})$ when $\mathbf{A}$ and $\mathbf{B}$ are of sizes $(N_\mathbf{A} \times M_\mathbf{A})$ and $(N_\mathbf{B} \times M_\mathbf{B})$, respectively. Now, the independent objective functions $\mathbf{P}_i^{\alpha_i}(\mathbf{m}_i)$, for $i = 1, 2$, in (2), are replaced by the coupled nonlinear function $\mathbf{P}^{(\alpha,\lambda)}(\mathbf{m})$

$$\mathbf{P}^{(\alpha,\lambda)}(\mathbf{m}) = \|\mathbf{W}_\mathbf{d}(\mathbf{G}\mathbf{m} - \mathbf{d}^{\mathrm{obs}})\|_2^2 + \alpha^2\|\mathbf{W}(\mathbf{m} - \mathbf{m}^{\mathrm{apr}})\|_2^2 + \lambda^2\|\mathbf{t}(\mathbf{m})\|_2^2. \tag{5}$$

Here the data vectors and model parameters are stacked in vectors $\mathbf{d}^{\mathrm{obs}} = \text{block\_stack}\ (\mathbf{d}_1^{\mathrm{obs}}, \mathbf{d}_2^{\mathrm{obs}}) \in \mathcal{R}^{2N}$, $\mathbf{m} = \text{block\_stack}\ (\mathbf{m}_1, \mathbf{m}_2) \in \mathcal{R}^{2M}$, respectively, and the matrices are block diagonal, $\mathbf{G} = \text{block\_diag}\ (\mathbf{G}_1, \mathbf{G}_2) \in \mathcal{R}^{2N\times 2M}$, $\mathbf{W}_\mathbf{d} = \text{block\_diag}\ (\mathbf{W}_{\mathbf{d}1}, \mathbf{W}_{\mathbf{d}2}) \in \mathcal{R}^{2N\times 2N}$ and $\mathbf{W} = \text{block\_diag}\ (\mathbf{W}_{\mathrm{depth}_1}\mathbf{W}_{\mathrm{h}1}\mathbf{W}_{\mathrm{L}1}, \mathbf{W}_{\mathrm{depth}_2}\mathbf{W}_{\mathrm{h}2}\mathbf{W}_{\mathrm{L}2}) \in \mathcal{R}^{2M\times 2M}$. The weighting matrices for hard constraints, L_1-norm regularization and depth weighting, are defined as before for each of the magnetic susceptibility and density terms. The distinction, now, between the formulation

13652478, 2022, 9, Downloaded from https://onlinelibrary.wiley.com/doi/10.1111/1365-2478.13265 by Arizona State University Acq & Analysis, Lib Continuations, Wiley Online Library on [19/10/2022]. See the Terms and Conditions (https://onlinelibrary.wiley.com/terms-and-conditions) on Wiley Online Library for rules of use; OA articles are governed by the applicable Creative Commons License

that is used for independent inversions, is the introduction of the nonlinear cross-gradient similarity constraint $\mathbf{t} = \nabla\mathbf{m}_1 \times \nabla\mathbf{m}_2 \in \mathcal{R}^{3M}$. Here ∇ is the gradient operator. The structural similarity is achieved when $\mathbf{t}(\mathbf{m}) = 0$; Gallardo and Meju (2003); provided that the similarity is supported by the data. Equivalently, although it is assumed that both models have similar structures at similar locations, it is also possible for one model to have a structure in a location where the other model has none. The scalar Lagrange parameter λ provides a relative weight on the cross-gradient term. The solutions, $\mathbf{m}_1$ and $\mathbf{m}_2$, are obtained by the minimization of the objective function (5) with respect to the bound constraints on each model parameter as

$$\mathbf{m}(\alpha, \lambda) = \underset{\substack{\mathbf{m}_1^{\min} \le \mathbf{m}_1 \le \mathbf{m}_1^{\max} \\ \mathbf{m}_2^{\min} \le \mathbf{m}_2 \le \mathbf{m}_2^{\max}}}{\operatorname{argmin}} \{\mathbf{P}^{(\alpha,\lambda)}(\mathbf{m})\}. \quad (6)$$

To determine the optimal choice for $\mathbf{m}$ from (6), an iterative process is required to find the minimum of the non-linear objective function $\mathbf{P}^{(\alpha,\lambda)}(\mathbf{m})$. The iteration is obtained by applying stationarity on the linear system that arises from linearizing the objective function about a starting model, in conjunction with a first-order Taylor expansion to linearize the cross-gradient term (Vatankhah et al., 2022). The resulting system of linear equations is symmetric positive definite, and its solution can be found using the conjugate gradient algorithm. Furthermore, it is possible to apply an alternating algorithm in which updates for the magnetic susceptibility and density are alternated at each iteration. This reduces the total computational cost and storage requirements and makes it possible to use algorithms even for large-scale problems. It has demonstrated that the algorithm can produce sparse density and magnetic susceptibility models, simultaneously, with structures that are as similar as possible (Vatankhah et al., 2022).

Estimating the scalar parameters

The regularization parameter α in an independent inversion and parameters $\alpha = [\alpha_1; \alpha_2]$, in the joint inversion, determine the relative weights for the stabilizer terms. Additionally, the parameter λ provides a relative weight for the cross-gradient coupling. The choice of these parameters is significant and impacts the convergence of the algorithms and the final reconstructed models. For an independent inversion, given an estimate of the SVD, or randomized SVD, of the sensitivity matrix, it is not expensive to use an automatic parameter-choice rule to find an optimal α. The application of methods for estimating α for individual potential field inversion, not repeated here, is described in Vatankhah et al. (2017). For example, the method of unbiased predictive risk estimation (Vogel, 2002) can be used to find approximately optimum regularization parameters for individual inversions of magnetic and gravity datasets, in which the optimal α are defined to reduce the estimate of the bias in the predicted solution(s).

On the other hand, the efficient and automatic determination of α_1, α_2 and λ is challenging. Hence for joint inversion, we adopt the approach in which initial large values are chosen for α_1 and α_2, with a slow cooling strategy at subsequent iterations given by

$$\alpha_i^{(k)} = q_i \alpha_i^{(k-1)}, \quad i = 1, 2. \quad (7)$$

where the cooling, specifically regularization parameter reduction, is stopped when the predicted data for one of the reconstructed models satisfies the observed data at the noise level. At this point, the relevant parameter is held fixed for the following iterations, while the other parameter continues to decrease. The iteration terminates when the χ^2 test given by (4) is satisfied independently for both predicted datasets. In this paper, we use $q_1 = 0.95$ and $q_2 = 0.9$. In the implementation, the Lagrange parameter λ is held fixed. This means that we gradually increase the impact of the cross-gradient constraint, as the $\alpha_i^{(k)}$ decreases with k. We should note that, for small λ, the cross-gradient constraint is only weakly applied and we would anticipate only limited similarity between the reconstructed models. On the other hand, if λ is too large, the algorithm will not converge. It is crucial, therefore, that λ is selected carefully. A simple but effective approach to find an appropriate choice for λ is to first run the algorithm with a small value and assess whether the algorithm is converging in a moderate number of iterations. When this is the case, the algorithm can be rerun with a larger value for λ and the process repeated. Generally, we see that if λ becomes too large, convergence is not achieved. Hence we use the smallest λ which provides both reasonable convergence and provides similarity between the reconstructed models.

GRAVITY AND MAGNETIC DATA

In this study, we used the ground magnetic and gravity data obtained over BK54 and BK55 kimberlite pipes within the Orapa kimberlite field (OKF) in Botswana. The OKF is one of the major diamond-producing regions in the world. Figure 1 shows the geology of the region and the location of OKF with the known kimberlites and diamond mines in Botswana. The OKF lies within the Kalahari basin, which trends northeast across central Botswana. The Kalahari basin is comprised of the Karoo Supergroup, which consists of a series of mostly clastic sediments interbedded with basaltic layers within a number of groups. Underlying the Karoo Supergroup is a series of Archean-aged lithologies, which include biotite gneisses, amphibolites and metamorphosed

13652478, 2022, 9, Downloaded from https://onlinelibrary.wiley.com/doi/10.1111/1365-2478.13265 by Arizona State University Acq & Analysis, Lib Continuations, Wiley Online Library on [19/10/2022]. See the Terms and Conditions (https://onlinelibrary.wiley.com/terms-and-conditions) on Wiley Online Library for rules of use; OA articles are governed by the applicable Creative Commons License

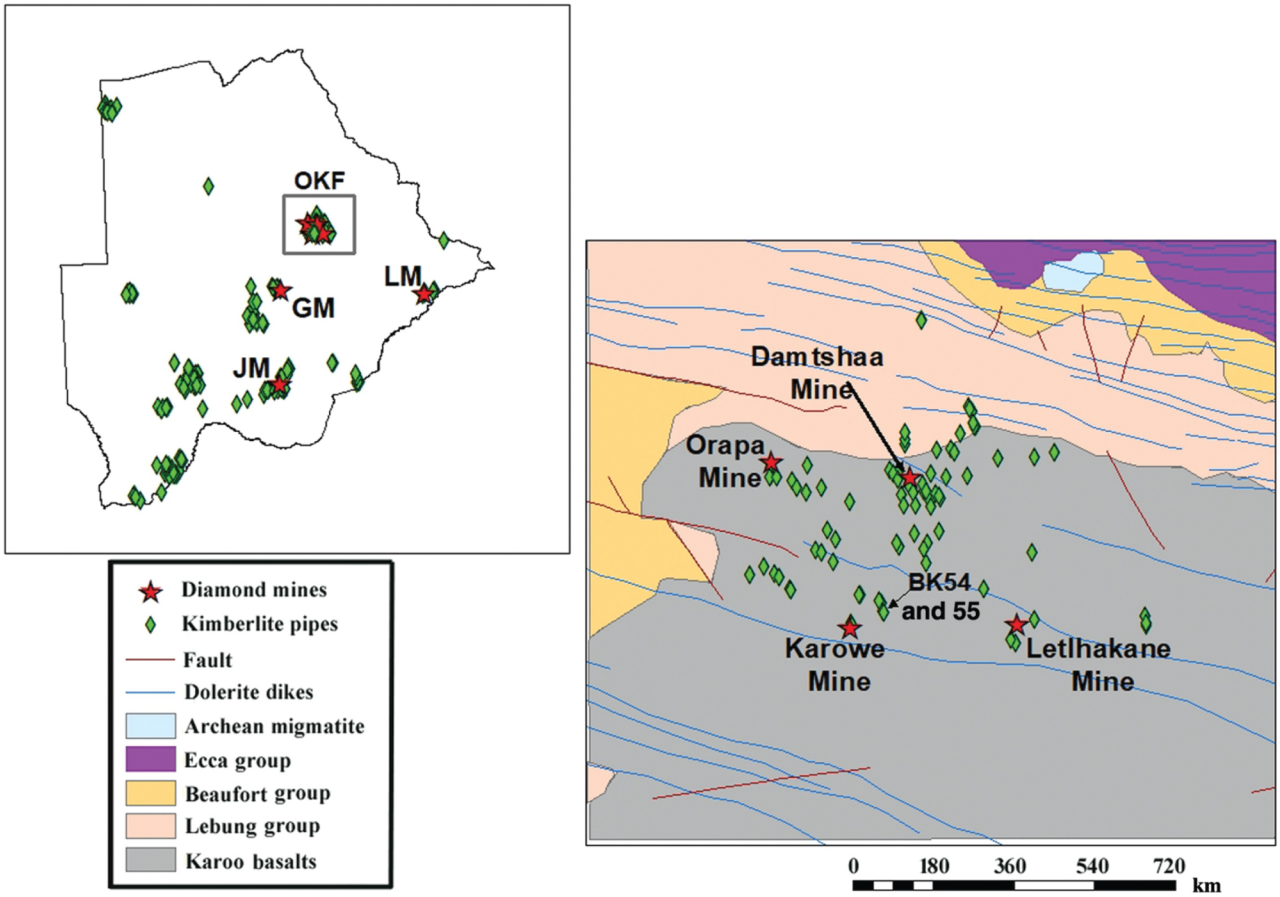

FIGURE 1 Top left: Location of kimberlites and diamond mines in Botswana. The Orapa kimberlite field is outlined with the black box. Right: Geologic map of the study area showing the location of the BK54 and BK55 kimberlite pipes in relation to the nearby diamond mines and kimberlite pipes (adopted from Matende & Mickus, 2021).

basalts (greenstones) (Matende & Mickus, 2021). Of importance to our study are the basalt flows of the Stromberg Group, which overlies most of the sedimentary sequences. Overlying all of the sedimentary and basaltic layers is a thin, approximately 1 m thick, layer of calcrete and silcrete. More information on the geology of the region can be found in Matende and Mickus (2021). Exploration for the diamond potential of the kimberlites includes several boreholes that helped define the depth of the different lithologies (silcrete, calrete, basalt, sandstones) and the presence of kimberlitic material. The kimberlitic material was found at depths between approximately 80–150 m in BK54, and between 125 and 220 m in BK55. One borehole, drilled until a depth of 221 m, did not encounter the bottom of the BK55 pipe, which indicates that more extension is possible.

In the survey area, data were collected every 25 m for the gravity data and 10 m for the magnetic data. The profile spacing was 50 m for the gravity data and 25 m for the magnetic data. Figure 2 illustrates the distribution of the observation stations in the survey area for gravity and magnetic measurements. The gravity data were processed using a local base station, which was occupied every 1–2 h to determine a drift curve and the tidal correction. Free-air corrections were made using mean sea level as a datum. The Bouguer gravity correction was made using 2.67 g cm^{-3} as a Bouguer density and sea level as a datum. Terrain corrections were not needed as the terrain is basically flat in the study area. The data were tied into the International gravity Net at an absolute gravity station in Gaborone. The Bouguer anomaly is shown in Figure 2a. The magnetic data are averages of several recorded readings at each station, with the removal of diurnal variations using a local base station. The magnetic anomaly is also shown in Figure 2b. Further details about the processing of the gravity and magnetic data are given in Matende and Mickus (2021).

In order to analyse the anomalies due to the kimberlites, the gravity and magnetic fields due to these features must be isolated (residual anomaly field). There are several ways to determine a residual anomaly, such as wavelength filtering, removal of polynomial surfaces and upward continuation. All of these methods were attempted, and the resultant maps were basically the same in terms of anomaly shapes and amplitudes. The removal of a polynomial trend surface is the easiest method to apply and does not have the ringing effect of wavelength filtering. Since the area is small, the regional field

13652478, 2022, 9, Downloaded from https://onlinelibrary.wiley.com/doi/10.1111/1365-2478.13265 by Arizona State University Acq & Analysis, Lib Continuations, Wiley Online Library on [19/10/2022]. See the Terms and Conditions (https://onlinelibrary.wiley.com/terms-and-conditions) on Wiley Online Library for rules of use; OA articles are governed by the applicable Creative Commons License

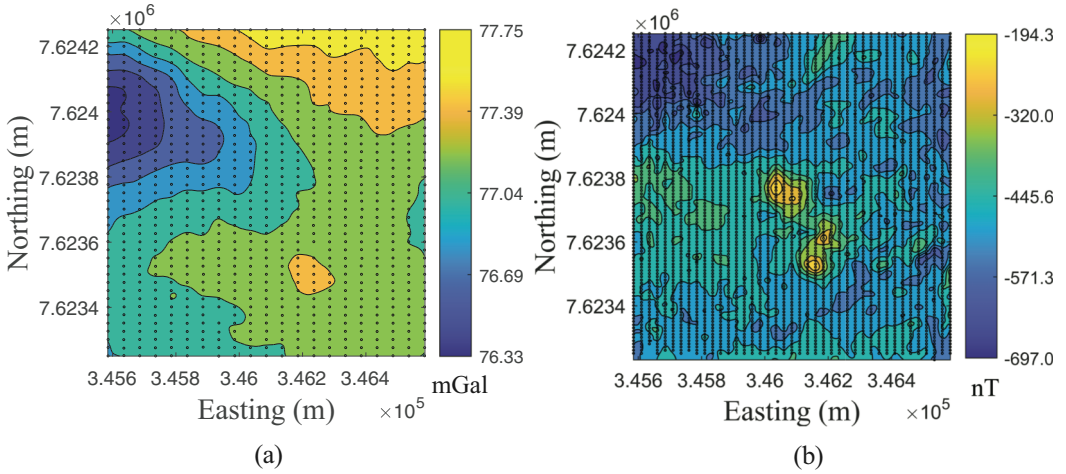

FIGURE 2 Location of the observation stations (black circles) in the survey area. In (a), the Bouguer gravity anomaly is shown. The stations are along the lines spaced 25 m apart and lines spaced 50 m apart. In (b), the magnetic anomaly is shown. Here, the stations are along the lines spaced 10 m apart and lines spaced 25 m apart.

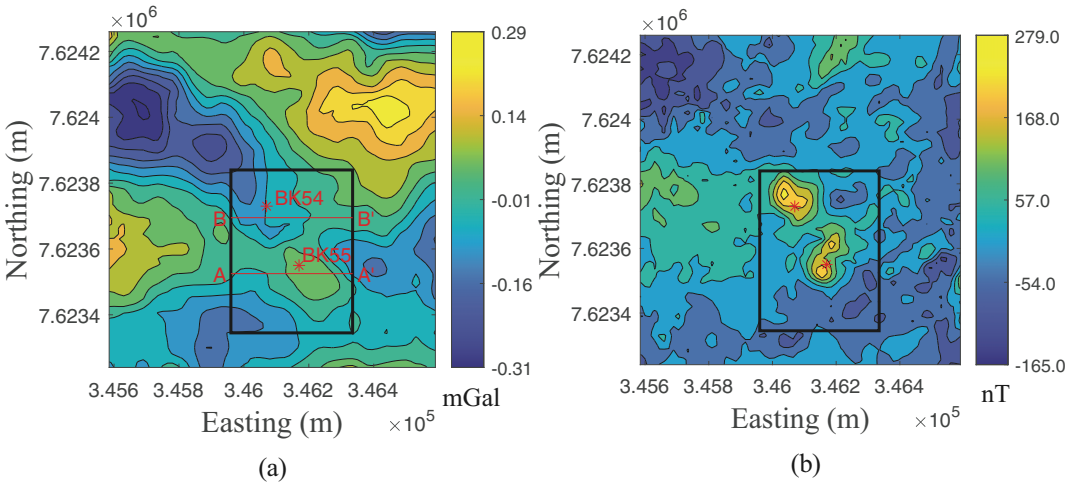

FIGURE 3 Residual gravity and magnetic anomalies over the study area. In (a), the residual gravity anomaly map was created by removing the third-order polynomial surface. In (b), the residual magnetic anomaly map was created by removing the first-order polynomial surface. The locations of two kimberlite pipes, BK54 and BK55, are illustrated with the red stars. The black rectangle indicates the area selected for inversion, for the same location for both anomalies. Lines AA′ and BB′ are the locations for which the cross sections of the reconstructed models will be illustrated.

should be relatively simple and it is therefore not justified to use a high-order polynomial. Thus, residual anomaly maps using orders 1, 2 and 3 were created, and these maps were basically similar in anomaly size and shape, so the inversions are not compromised by the specific selections. The resultant residual gravity and magnetic anomaly maps using orders 3 and 1 are shown in Figure 3a and 3b, respectively. We should note here that the data which are used in this study are the same as those used by Matende and Mickus (2021).

The residual magnetic anomaly map clearly indicates two magnetic maxima over the kimberlite lithologies found from boreholes in BK54 and BK55. Other positive anomalies, especially in the west, may be related to near-surface basalt or magnetic lithologies within the Precambrian basement. The residual gravity anomaly map indicates a positive, approximately circular, anomaly over BK55 occurring mainly to the southeast of the borehole. The BK54 pipe is located on the edge of a relatively large amplitude gravity minimum and is not associated with a gravity maximum. This may be due to the crater facies containing less dense material (Matende & Mickus, 2021). The absence of a distinctive anomaly may also be due to a lack of density contrast between the BK54 pipe and the surrounding sandstones. The individual magnetic and gravity inversions presented in Matende and Mickus (2021) provided valuable information about the subsurface lithological structures. Their results indicate that BK54 is smaller

13652478, 2022, 9, Downloaded from https://onlinelibrary.wiley.com/doi/10.1111/1365-2478.13265 by Arizona State University Acq & Analysis, Lib Continuations, Wiley Online Library on [19/10/2022]. See the Terms and Conditions (https://onlinelibrary.wiley.com/terms-and-conditions) on Wiley Online Library for rules of use; OA articles are governed by the applicable Creative Commons License

in volume than BK55 and that neither pipe is thicker than 125 m. Further, they explained that the difference in shape and the lack of a gravity anomaly over BK54 may imply a different formation mechanism for each kimberlite pipe. On the other hand, although several mechanisms can explain the formation of the kimberlites, BK54 may have been formed by a more explosive eruption producing more tuffistic material in the crater and diatreme facies (Matende & Mickus, 2021). To assess whether it is feasible to improve the modelling of the subsurface structures, we also present the results for the individual, but sparse, magnetic and gravity inversions, over the BK54 and BK55 pipes, in sections Inverting the Magnetic Data Independently and Inverting the Gravity Data Independently, respectively. Further, in the section Joint Inversion of the Data the results of joint focusing inversion are also presented.

INVERSION RESULTS

To perform the inversions, we have selected an area including BK54 and BK55 pipes, as indicated by the black rectangle in Figure 3. The selected residual magnetic and gravity anomalies were re-gridded at a 15-m spacing yielding $26 \times 34 = 884$ data points. To be clear, here we use a local coordinate system in which the data point on the southwest corner of the selected area has coordinates (0,0). The coordinates of all other data points and the model geometry are measured with respect to this point. For the inversion, we consider a model which extends to a depth of 300 m. The subsurface under the data grid is divided into $26 \times 34 \times 20$ prisms with a size of 15 m in each dimension. Further, to avoid possible distortion in the reconstruction along the boundaries, it is necessary to add padding to the domain. Here we add padding of width 45 m in the east, west, south, and north directions, corresponding to an extra three prisms in these directions, yielding a model domain with $32 \times 40 \times 20 = 25,600$ prisms. We assume that each datum j has an error with standard deviation $(\tau_1 |(\mathbf{d}_i^{\text{obs}})_j| + \tau_2 \max |\mathbf{d}_i^{\text{obs}}|)$, $i = 1, 2$ and $j = 1 \cdots N$. The parameter pair (τ_1, τ_2) is selected as $(0.01, 0.03)$ and $(0.01, 0.01)$ for magnetic and gravity datasets, respectively. In the survey area, the intensity of the geomagnetic field and its inclination and declination are 28,625 nT, $-62.1°$, and $-13.5°$, respectively. For all inversions presented here, the a priori model is assumed to be zero. Imposed-bound constraints for the magnetic susceptibility, $0 \leq \kappa \leq 0.04$ in SI units were determined based on magnetic susceptibility logs available in the area (Matende & Mickus, 2021). For identifying suitable constraints on the density, no density logs were measured in the survey area but the amplitude of the observed gravity anomaly indicates targets with low-density contrast. This is also confirmed in the results obtained by Matende and Mickus (2021). Consequently, the results presented are obtained using the bound constraints $-0.08 \leq \rho \leq 0.06$ in units g cm^{-3}. Further, it is assumed there is no remanent magnetization and that self-demagnetization effects are negligible (Matende & Mickus, 2021). Computations are performed on a laptop computer with an Intel(R) Core i7-10750 CPU 2.60 GHz processor and 16 GB RAM.

Inverting the magnetic data independently

The independent inversion of magnetic data using the L_1-norm algorithm terminates after eight iterations, and the computational cost, measured with respect to time only, is about 21 s. The misfit measure at iteration 8 is 0.81. Based on the convergence criteria applied, this also means that the value at iteration 7 is greater than 1. A substantially smaller value than 1 would indicate a solution that overfits the data, but values greater than 1 indicate that the algorithm has not converged to the desired noise level. Figure 4 illustrates three depth slices of the reconstructed magnetic susceptibility model at 70, 110 and 150 m. Additionally, two cross sections of the model, over BK55 and BK54, are shown in Figure 5. The results indicate sharp and focused images for both pipes. These results suggest that the tops of the pipes are at depths ranging from 30 to 45 m. These depths are not consistent with the borehole information; which indicate that the upper levels of BK54 and BK55 are at approximately 80 and 125 m, respectively. On the other hand, the extents of the pipes are consistent with the drillhole data and suggest that BK54 extends to at least 150 m and BK55 to approximately 220 m in depth. The presented results using the focusing inversion are different from those obtained using the smooth inversion algorithm given in Matende and Mickus (2021). Therefore, it is suggested that BK54 and BK55 extend even deeper. This may be due to the application of a smooth, rather than an L_1, constraint in the inversion algorithm. We also see from Figure 5b that BK54 at depth and on the western side of the pipe may be connected to another magnetically susceptible structure that is near the bottom of the pipe. This may be related to magnetic susceptible minerals in the Archean lithologies. Moreover, the magnetic susceptibility structure is suggested on the west side of BK55 at depth, but there is no clear connection between the pipe and this structure. The magnetic anomaly produced by the reconstructed model, illustrated in Figure 6b is in good agreement with the observed anomaly at the predefined noise level. Finally, Figure 6c illustrates the data residual, which is the difference between the observed and predicted datasets, normalized by the assigned uncertainties. A histogram of the errors, not presented here, indicates a Gaussian distribution with approximately zero mean.

13652478, 2022, 9, Downloaded from https://onlinelibrary.wiley.com/doi/10.1111/1365-2478.13265 by Arizona State University Acq & Analysis, Lib Continuations, Wiley Online Library on [19/10/2022]. See the Terms and Conditions (https://onlinelibrary.wiley.com/terms-and-conditions) on Wiley Online Library for rules of use; OA articles are governed by the applicable Creative Commons License

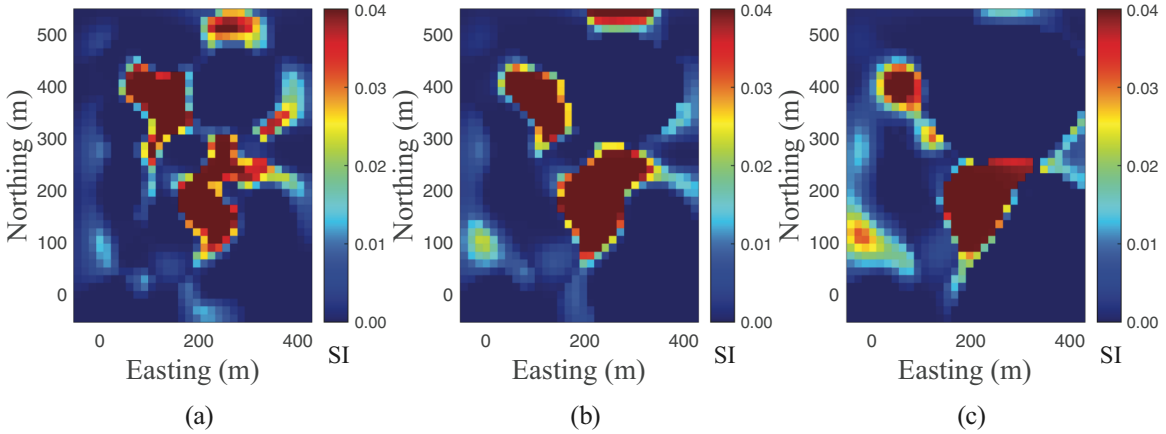

FIGURE 4 Reconstructed magnetic susceptibility model using independent focusing inversion for the magnetic data shown in Figure 6a. The depth slices are at 70, 110, and 150 m in (a), (b), and (c), respectively.

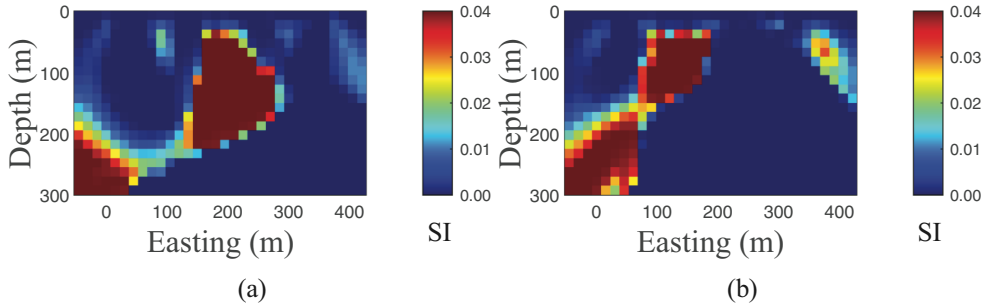

FIGURE 5 Reconstructed magnetic susceptibility model using independent focusing inversion for the magnetic data shown in Figure 6a. The cross sections are at northing = 180 m (line AA′ in Figure 3a) and northing = 350 m (line BB′ in Figure 3a) in (a) and (b), respectively.

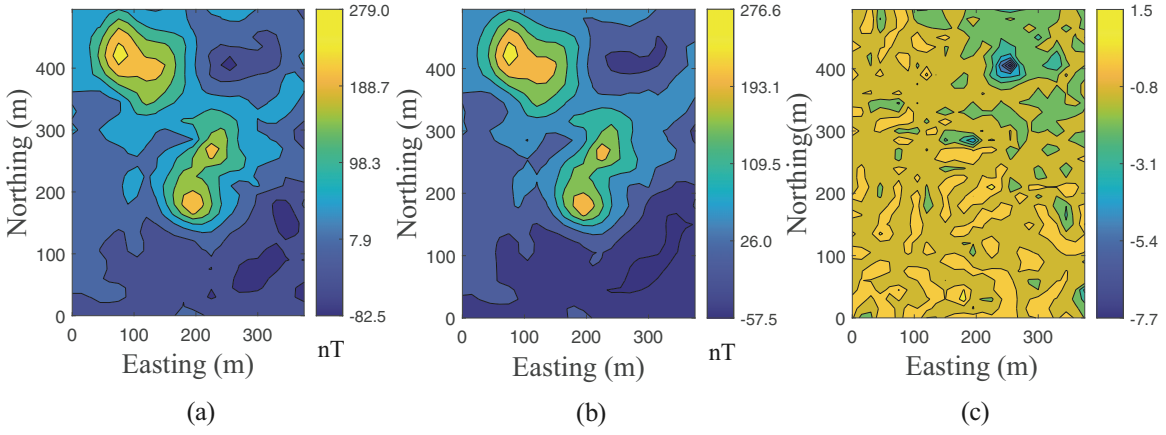

FIGURE 6 In (a), the total magnetic intensity data selected for the inversion and in (b) the data produced by the reconstructed model in Figure 4. The contour intervals are 50 nT. In (c), the data residual, the difference between the (a) and (b), normalized by the assigned uncertainties, is presented. The residual demonstrates that the normalized error is concentrated around 0, with moderate departures from the observed anomaly in the northeast corner, as is also evident immediately by comparing the two independent contour plots.

13652478, 2022, 9, Downloaded from https://onlinelibrary.wiley.com/doi/10.1111/1365-2478.13265 by Arizona State University Acq & Analysis, Lib Continuations, Wiley Online Library on [19/10/2022]. See the Terms and Conditions (https://onlinelibrary.wiley.com/terms-and-conditions) on Wiley Online Library for rules of use; OA articles are governed by the applicable Creative Commons License

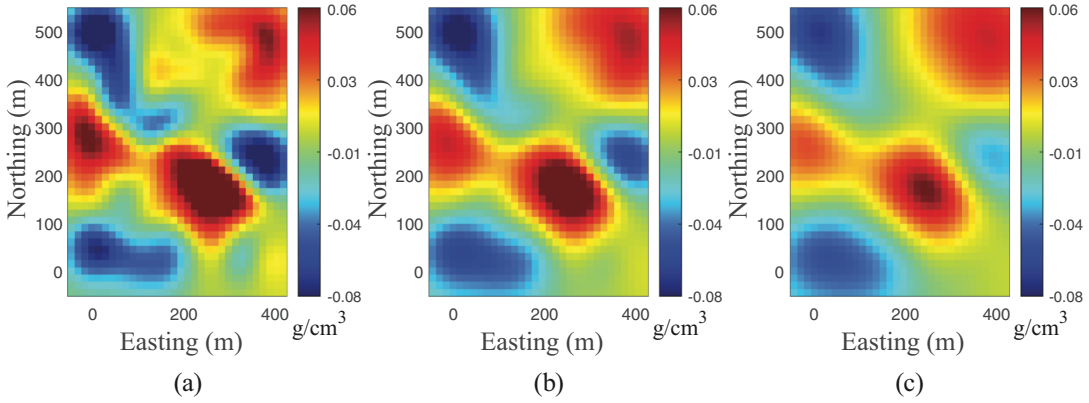

FIGURE 7 Reconstructed density model using independent focusing inversion for the gravity data shown in Figure 9a. The depth slices are at 70, 110, and 150 m in (a), (b) and (c), respectively.

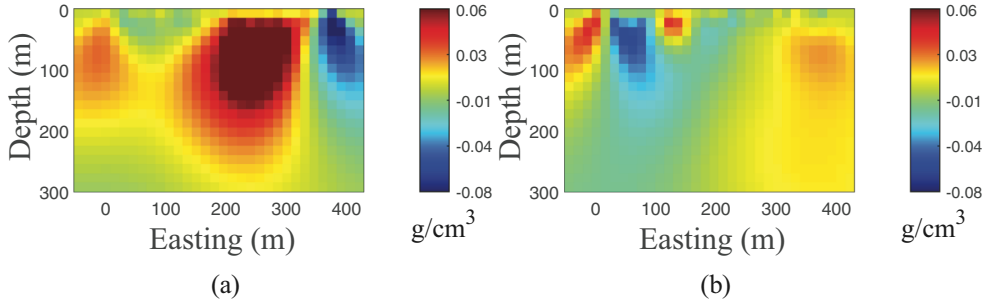

FIGURE 8 Reconstructed density model using independent focusing inversion for the gravity data shown in Figure 9a. The cross sections at northing = 180 m (line AA′ in Figure 3a) and northing = 350 m (line BB′ in Figure 3a) are shown in (a) and (b), respectively.

Inverting the gravity data independently

For the independent inversion of the gravity dataset, we find that the inversion terminates after five iterations, using just 15 s of CPU time. The misfit measure is 0.99. The reconstructed density model is shown in three depth slices at 70, 110 and 150 m (Figure 7). Additionally, two cross sections over BK55 and BK54 are also shown in Figure 8. As seen in Figures 7 and 8, the algorithm could not produce a sparse model. To verify that the *lack of success* in the inversion is not due to chosen parameter settings, the inversion was repeated for multiple settings of the parameters and with different bound constraints. Similar results are obtained in all cases. None of the experiments are able to provide a result that is as compact as we see with the inversion of the magnetic data. This is probably due to the lack of the spatial resolution in the gravity data. As we already noted, the gravity data were collected with a 25-m station spacing along profiles spaced 50 m apart. The spatial resolution is less than that for the magnetic data and may not be high enough to produce a focused image. Additionally, if the regional gravity field is incorrect this may contribute to the difficulty with obtaining a satisfactory inversion. On the other hand, as clarified in the section Gravity and Magnetic Data, multiple distinct approaches were used to find the regional gravity fields. In all cases, the residual gravity anomalies were similar in shape and amplitude to that given in Figure 3a.

Based on the results that we do obtain, for the gravity data, some conclusions are still possible. We see that for the BK54 pipe, as anticipated from the given anomalies, the algorithm could not reconstruct a clear geometry for the target. There are lower density materials associated with BK54, but the model does not clearly indicate a specific target. As noted by Matende and Mickus (2021), the low-density area is probably crater fill related to the formation of the pipe. Here, the higher density material above the known position of the kimberlite is probably due to an overlying basalt. The BK55 pipe extends from a depth of approximately 15 m to more than 220 m. In contrast with the magnetic susceptibility inverse model, the density model has a major axis of the pipe that trends to the northwest. Integrating the results of the magnetic and gravity data inversion, however, provided valuable information about the geometry and physical properties of the BK54 and BK55 pipes. The data produced by the reconstructed density model is shown in Figure 9b. Finally, the data residual, that is, the difference between the observed and predicted

13652478, 2022, 9, Downloaded from https://onlinelibrary.wiley.com/doi/10.1111/1365-2478.13265 by Arizona State University Acq & Analysis, Lib Continuations, Wiley Online Library on [19/10/2022]. See the Terms and Conditions (https://onlinelibrary.wiley.com/terms-and-conditions) on Wiley Online Library for rules of use; OA articles are governed by the applicable Creative Commons License

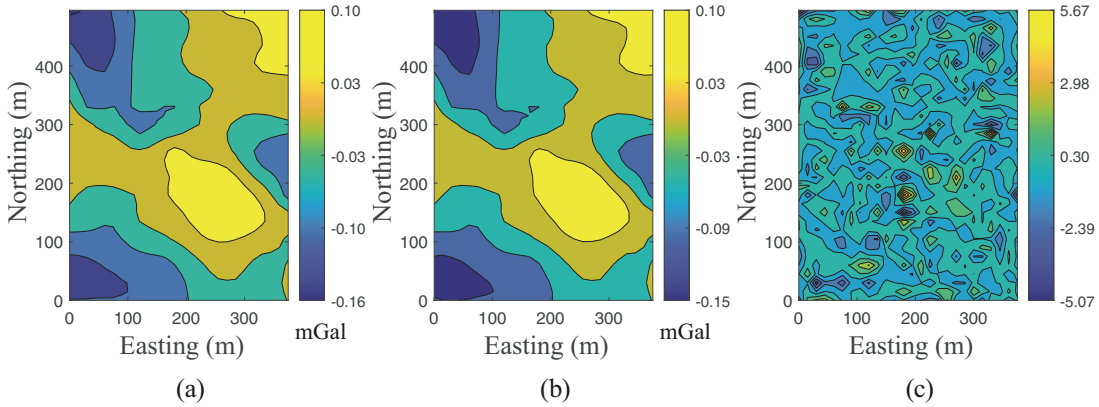

FIGURE 9 (a) The residual gravity data selected for the inversion and (b) the anomaly produced by the reconstructed model in Figure 7. The contour intervals are 0.05 mGal. In (c), the data residual, the difference between the (a) and (b), normalized by the assigned uncertainties, is presented. The contour plot very clearly shows that the errors are distributed around 0 and are approximately normally distributed for the entire area.

datasets, normalized by the assigned uncertainties, is shown in Figure 9c. A histogram of errors, not presented here, indicates a Gaussian distribution with approximately zero mean.

Joint inversion of the data

The final step was to perform a simultaneous joint inversion on the magnetic and gravity datasets. The inversion terminated after 86 iterations with a computational cost of approximately 6461 s, which is considerably more than for the independent inversions. There are a number of factors that increase the cost. First, we note that the set of unknown parameters for the two datasets is of course doubled to $2M$ as compared to M and the sensitivity matrices are larger. For our codes, however, we use the Fast Fourier transform for both forward and transpose operations with $\mathbf{G}_i$, and rather than storing the full matrix of MN elements in each case we only need to store a transform requiring $\mathcal{O}(N)$ entries. Consequently, the cost of these operations with $\mathbf{G}_i$, using the transform implementation rather than the actual matrix, is much reduced, particularly for large M (Hogue et al., 2020). On the other hand, the cross-gradient vector and its Jacobian matrix are needed at each iteration. This dramatically increases the computational demand because the Jacobian matrix requires large memory, and all its entries must be calculated at each iteration of the joint inversion. Second, for the independent inversion, we use the method of unbiased predictive risk estimation to automatically find the respective regularization parameters α_i, which is not possible when solving for the joint inversion. Indeed, there is in general no automatic approach to find λ. The algorithm uses the cooling strategy for α_i and a fixed choice for λ, based on experimental verification. Thus, the iteration converges more slowly and at a higher computational cost per iteration.

Figure 10 illustrates three depth slices of the reconstructed magnetic susceptibility and density models at 70, 110 and 150 m. Additionally, two cross sections over BK55 and BK54 are also shown in Figure 11. The results verify that the joint inversion algorithm, with the cross-gradient constraint, seeks to produce density and magnetic susceptibility models that are structurally similar. It is also clear that the jointly reconstructed models share not only structural similarity but also sparsity. Although the magnetic susceptibility model exhibits reduced sparsity from this approach, the density model now exhibits some sparsity and is more compact than was obtained by independent inversion. The shapes of the reconstructed models in each case are different from those obtained by independent inversions. The jointly obtained result for the magnetic susceptibility is now close to the drill hole information that the upper depth for BK54 is at 45 m. Further, contrasting the models in Figures 5b and 11b, we see that the BK54 pipe is now connected with the structure at depth. On the other hand, the jointly reconstructed density model does not show a clear target for BK54, although it is clear that there is a low-density target that is similar to the distribution of the magnetic susceptibility located in the BK54 region. In relation to the BK55, the magnetic susceptibility and density distributions obtained jointly indicate that the pipe extends from 30 m to approximately 200 m and is roughly cone shaped in structure. The magnetic susceptibility result, however, now suggests that the BK55 may be consisting of two structures, the smallest of which is located to the northeast of the larger. Since this observation is not confirmed by analysis of the obtained density models, it suggests that further drilling is needed in the area, or that data should be obtained at higher resolutions. The predicated anomalies produced by the reconstructed models are illustrated in Figure 12. Finally, the data residuals, normalized by the assigned uncertainties, are illustrated in Figure 13.

13652478, 2022, 9, Downloaded from https://onlinelibrary.wiley.com/doi/10.1111/1365-2478.13265 by Arizona State University Acq & Analysis, Lib Continuations, Wiley Online Library on [19/10/2022]. See the Terms and Conditions (https://onlinelibrary.wiley.com/terms-and-conditions) on Wiley Online Library for rules of use; OA articles are governed by the applicable Creative Commons License

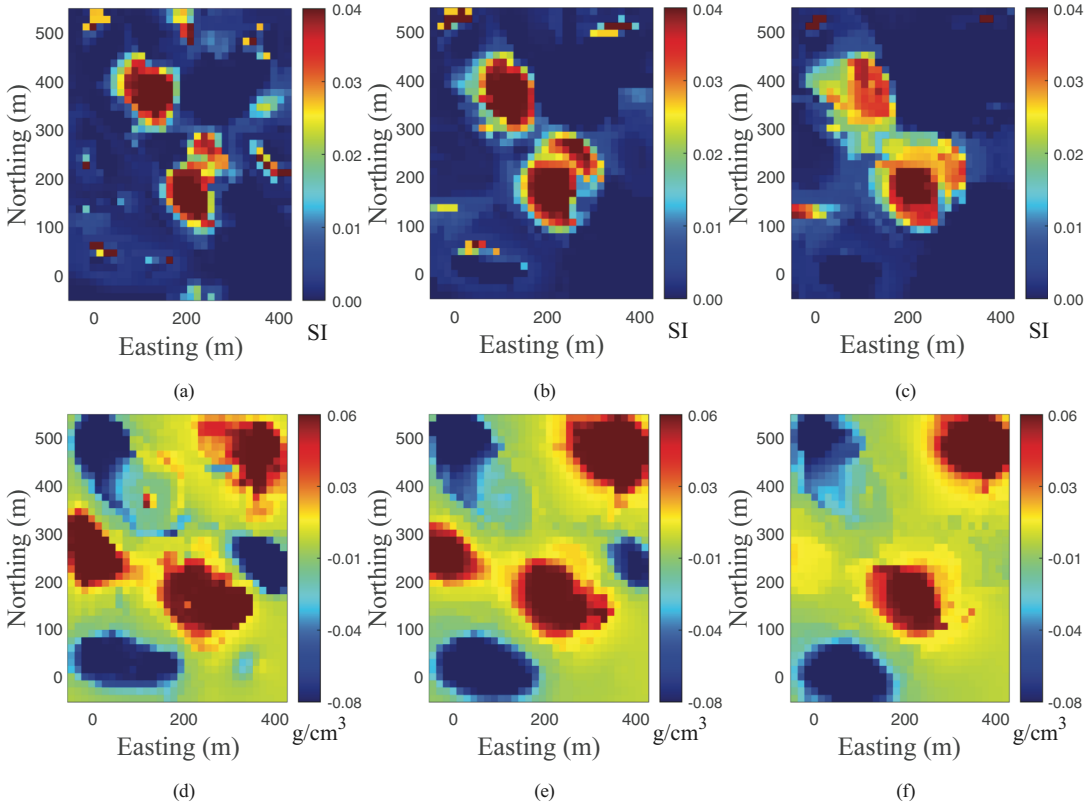

FIGURE 10 Reconstructed models using joint focusing inversion for the datasets are given in Figures 6a and 9a. The depth slices are at 70, 110, and 150 m as shown in (a), (b) and (c) for the magnetic susceptibility and in (d), (e) and (f) for the density, respectively.

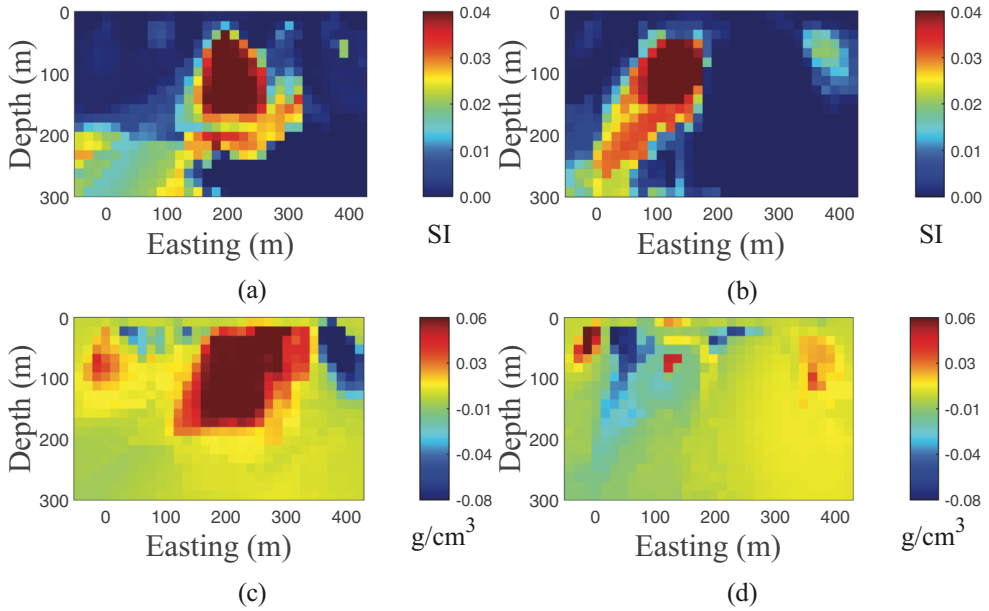

FIGURE 11 Reconstructed models using joint focusing inversion algorithm for the datasets given in Figures 6a and 9a. (a) and (b) show the magnetic susceptibility model, and (c) and (d) show the density model. The cross sections are at northing = 180 m for 11(a) and (c) and northing = 350 m for (b) and (d), respectively.

13652478, 2022, 9, Downloaded from https://onlinelibrary.wiley.com/doi/10.1111/1365-2478.13265 by Arizona State University Acq & Analysis, Lib Continuations, Wiley Online Library on [19/10/2022]. See the Terms and Conditions (https://onlinelibrary.wiley.com/terms-and-conditions) on Wiley Online Library for rules of use; OA articles are governed by the applicable Creative Commons License

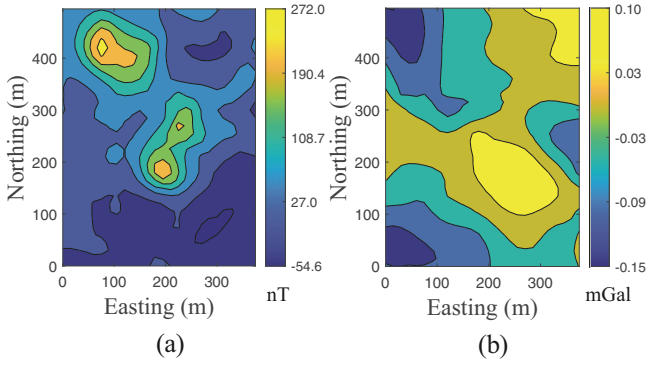

FIGURE 12 In (a) the magnetic anomaly produced by the reconstructed susceptibility model, and in (b) the gravity anomaly produced by the reconstructed density model.

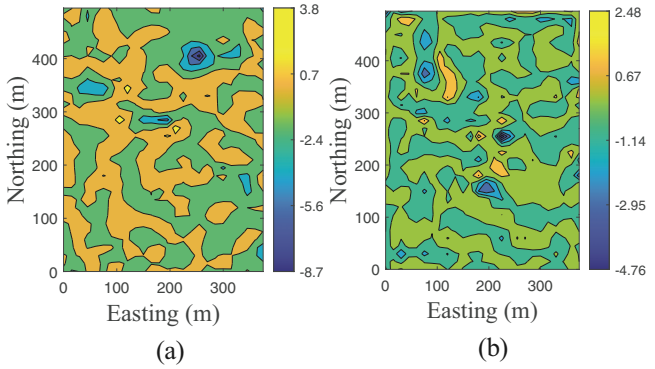

FIGURE 13 Data residual, differences between observed and predicted data, normalized by the assigned uncertainties. (a) for the total magnetic field shows the difference between Figures 6a and 12a, and (b) for the gravity anomalies shows the difference between Figures 9a and 12b.

CONCLUSION

We investigated the independent and joint focusing inversion algorithms, based on L_1-norm stabilization on the magnetic and gravity data obtained over the BK54 and BK55 kimberlites pipes in Botswana. The magnetic data are high resolution and, clearly, indicates two pipes. But the spatial resolution of the gravity data is relatively low. The BK54 pipe does not appear on the residual gravity anomaly, while the BK55 is characterized by a positive gravity anomaly. We showed that the independent inversion of magnetic data can produce a focused image of the subsurface. The BK54 and BK55 pipes are reconstructed with sharp boundaries. The depths to the top of the pipes start from 30 to 45 m and are not consistent with the drillhole information, but the extensions in depth are close to those estimated by boreholes. Here, BK54 shows a southeast-northwest extension, but the trend of BK55 is in the southwest-northeast direction. On the other hand, the independent gravity algorithm can only reconstruct the geometry of the BK55 pipe. Some lower density materials appear at the location of the BK54 pipe but do not indicate a specific target. Moreover, the reconstructed model for the BK55 pipe is not focused. We believe that the problem originates from the lack of resolution in the available data. Here, the BK55 pipe extends from depth 15 to 210–220 m. In contrast with the magnetic susceptibility reconstruction, the major axis of the pipe is in the southeast-northwest direction. Furthermore, the reconstructed density model for the BK55 pipe is wider than for the magnetic susceptibility model. This may be due to higher density material that is not related to the pipe or due to lower susceptibility values of the kimberlite pipe. Finally, we performed a joint focusing inversion based on the cross-gradient constraint. The algorithm produced, approximately, similar density and magnetic susceptibility models. In contrast to the magnetic susceptibility model obtained independently, the BK54 is now continuously connected with a structure at depth. Moreover, the jointly reconstructed models share a sparsity structure. The models are not as sparse as the independently obtained magnetic susceptibility model, but they are more compact than the independently obtained density model. Furthermore, the magnetic susceptibility model obtained via the joint inversion identifies two structures associated with BK55, the smallest one being located to the northeast of the other. The two distinct structures do not appear in the reconstructed density model. This contradiction suggests that more data need to be collected in the area either by drilling or by the collection of data at a higher resolution for inversion.

We have demonstrated that although it is possible to produce approximately similar models using a joint inversion, the quality of the solutions depends on datasets which are used. Finally, we demonstrated that independent inversion is computationally much more efficient than joint inversion, in terms of cost and memory. When using the joint inversion on two datasets, the cost of computing the cross-gradient term, and its Jacobian matrix, dramatically increases the per iteration cost as compared to the independent inversions. Further, the joint inversion requires many more iterations than the independent inversions because it is challenging to find an automatic process to fine-tune the associated regularization parameters. On the other hand, we can expect to have improved recovery of subsurface targets when using a joint inversion. Moreover, the joint inversion may be used to indicate locations where additional data collection could be useful for yielding a higher resolution of subsurface structures.

ACKNOWLEDGEMENTS

We would like to acknowledge the Editor Dr. Giovanni Florio, associate editor and two anonymous reviewers for their helpful suggestions which assisted us to improve this manuscript.

13652478, 2022, 9, Downloaded from https://onlinelibrary.wiley.com/doi/10.1111/1365-2478.13265 by Arizona State University Acq & Analysis, Lib Continuations, Wiley Online Library on [19/10/2022]. See the Terms and Conditions (https://onlinelibrary.wiley.com/terms-and-conditions) on Wiley Online Library for rules of use; OA articles are governed by the applicable Creative Commons License

DATA AVAILABILITY STATEMENT

The data that support the findings of this study are available from the corresponding author upon reasonable request.

ORCID

Saeed Vatankhah https://orcid.org/0000-0001-7403-6848
Shuang Liu https://orcid.org/0000-0001-9184-0782

REFERENCES

Barbosa, V.C.F. & Silva, J.B.C. (1994) Generalized compact gravity inversion. *Geophysics*, 59(1), 57–68.

Boulanger, O. & Chouteau, M. (2001) Constraints in 3D gravity inversion. *Geophysical Prospecting*, 49(2), 265–280.

Cella, F. & Fedi, M. (2012) Inversion of potential field data using the structural index as weighting function rate decay. *Geophysical Prospecting*, 60(2), 313–336.

Constable, S.C., Parker, R.L. & Constable, C.G. (1987) Occam's inversion: a practical algorithm for generating smooth models from electromagnetic sounding data. *Geophysics*, 52(3), 289–300.

Costa, A. (1989) Palmietfontein kimberlite pipe, South Africa – a case history. *Geophysics*, 54(6), 689–700.

Devriese, S.G.R., Davis, K. & Oldenburg, D.W. (2017) Inversion of airborne geophysics over the do-27/do-18 kimberlites-part 1: potential fields. *Interpretation*, 5(3), T299–T311.

Field, M. & Scott Smith, B.H. (1999) Contrasting geology and near-surface emplacement of kimberlite pipes in southern Africa and Canada. In: *Proceedings of the 7th International Kimberlite Conference*. Cape Town, South Africa: Red Roof Design, pp. 214–237.

Fournier, D. & Oldenburg, D.W. (2019) Inversion using spatially variable mixed ℓ_p norms. *Geophysical Journal International*, 218(1), 268–282.

Fregoso, E. & Gallardo, L.A. (2009) Cross-gradients joint 3D inversion with applications to gravity and magnetic data. *Geophysics*, 74(4), L31–L42.

Fregoso, E., Gallardo, L.A. & García-Abdeslem, J. (2015) Structural joint inversion coupled with Euler deconvolution of isolated gravity and magnetic anomalies. *Geophysics*, 80(2), G67–G79.

Gallardo, L.A. & Meju, M.A. (2003) Characterization of heterogeneous near-surface materials by joint 2D inversion of DC resistivity and seismic data. *Geophysical Research Letters*, 30(13), 1658.

Gallardo, L.A. & Meju, M.A. (2004) Joint two-dimensional DC resistivity and seismic travel time inversion with cross-gradients constraints. *Journal of Geophysical Research: Solid Earth*, 109(B3), B03311.

Haber, E. & Holtzman Gazit, M. (2013) Model fusion and joint inversion. *Surveys in Geophysics*, 34, 675–695.

Haber, E. & Oldenburg, D. (1997) Joint inversion: a structural approach. *Inverse Problems*, 13(1), 63–77.

Hogue, J.D., Renaut, R.A. & Vatankhah, S. (2020) A tutorial and open source software for the efficient evaluation of gravity and magnetic kernels. *Computers & Geosciences*, 14, 104575.

Kamara, A.Y.S. (1981) Review: Geophysical methods for kimberlite prospecting. *Exploration Geophysics*, 12(3), 43–51.

Kjarsgaard, B.A. (2007) Review: Geophysical methods for kimberlite prospecting. In: *Proceedings of Exploration 07: Fifth Decennial International Conference on Mineral Exploration*. Toronto, Canada: The Conference, pp. 667–677.

LaFehr, T.R. & Nabighian, M.N. (2012) *Fundamentals of Gravity Exploration*. SEG Geophysical Monograph Series. Houston, TX: SEG.

Last, B.J. & Kubik, K. (1983) Compact gravity inversion. *Geophysics*, 48(6), 713–721.

Leliévre, P.G., Farquharson, C.G. & Hurich, C.A. (2012) Joint inversion of seismic traveltimes and gravity data on unstructured grids with application to mineral exploration. *Geophysics*, 77(1), K1–K15.

Li, Y. & Oldenburg, D.W. (1996) 3-D inversion of magnetic data. *Geophysics*, 61(2), 394–408.

Lin, W. & Zhdanov, M.S. (2018) Joint multinary inversion of gravity and magnetic data using Gramian constraints. *Geophysical Journal International*, 215(3), 1540–1557.

Masun, K.M., Doyle, B., Ball, S. & Walker, S. (2004) The geology and mineralogy of the Anuri kimberlite, Nunavut, Canada. *Lithos*, 76(1), 75–97.

Matende, K. & Mickus, K. (2021) Magnetic and gravity investigation of kimberlites in north-central Botswana. *Geophysics*, 86(2), B67–B78.

Moorkamp, M., Heincke, B., Jegen, M., Roberts, A.W. & Hobbs, R.W. (2011) A framework for 3-D joint inversion of MT, gravity and seismic refraction data. *Geophysical Journal International*, 184(1), 477–493.

Nielsen, L. & Jacobsen, B. (2000) Integrated gravity and wide-angle seismic inversion for 2-D crustal modelling. *Geophysical Journal International*, 140, 222–232.

Pettit, W. (2009) Geophysical signatures of some recently discovered large (>40 ha) kimberlites on the Alto Cuilo concession in northeastern Angola. *Lithos*, 112(1), 106–115.

Pilkington, M. (1997) 3-D magnetic imaging using conjugate gradients. *Geophysics*, 62(4), 1132–1142.

Portniaguine, O. & Zhdanov, M.S. (1999) Focusing geophysical inversion images. *Geophysics*, 64(3), 874–887.

Power, M. & Hildes, D. (2007) Geophysical strategies for kimberlite exploration in northern Canada. In: *Proceedings of Exploration 07: Fifth Decennial International Conference on Mineral Exploration*. Toronto, Canada: The Conference, pp. 1025–1031.

Sun, J. & Li, Y. (2014) Adaptive l_p inversion for simultaneous recovery of both blocky and smooth features in a geophysical model. *Geophysical Journal International*, 197(2), 882–899.

Sun, J. & Wei, X. (2021) Research note: Recovering sparse models in 3D potential-field inversion without bound dependence or staircasing problems using a mixed L_p norm regularization. *Geophysical Prospecting*, 69(4), 901–910.

Tryggvason, A. & Linde, N. (2006) Local earthquake (LE) tomography with joint inversion for P- and S-wave velocities using structural constraints. *Geophysical Research Letters*, 33(7), L07303.

Vatankhah, S., Liu, S., Renaut, R.A., Hu, X. & Baniamerian, J. (2020) Improving the use of the randomized singular value decomposition for the inversion of gravity and magnetic data. *Geophysics*, 85, G93–G107.

Vatankhah, S., Liu, S., Renaut, R.A., Hu, X., Hogue, J.D. & Gharloghi, M. (2022) An efficient alternating algorithm for the L_p-norm cross-gradient joint inversion of gravity and magnetic data using the 2-D fast Fourier transform. *IEEE Transactions on Geoscience and Remote Sensing*, 60, 1–16.

Vatankhah, S., Renaut, R.A. & Ardestani, V.E. (2017) 3-D projected ℓ_1 inversion of gravity data using truncated unbiased predictive risk estimator for regularization parameter estimation. *Geophysical Journal International*, 210(3), 1872–1887.

13652478, 2022, 9, Downloaded from https://onlinelibrary.wiley.com/doi/10.1111/1365-2478.13265 by Arizona State University Acq & Analysis, Lib Continuations, Wiley Online Library on [19/10/2022]. See the Terms and Conditions (https://onlinelibrary.wiley.com/terms-and-conditions) on Wiley Online Library for rules of use; OA articles are governed by the applicable Creative Commons License

Vatankhah, S., Renaut, R.A. & Liu, S. (2020) Research note: A unifying framework for the widely used stabilization of potential field inverse problems. *Geophysical Prospecting*, 68, 1416–1421.

Vogel, C.R. (2002) *Computational methods for inverse problems*. Philadelphia, PA: SIAM.

Zhdanov, M.S., Gribenko, A. & Wilson, G. (2012) Generalized joint inversion of multimodal geophysical data using Gramian constraints. *Geophysical Research Letters*, 39(9).

Zhdanov, M.S. & Tolstaya, E.V. (2004) Minimum support nonlinear parametrization in the solution of a 3D magnetotelluric inverse problem. *Inverse Problems*, 20, 937–952.

How to cite this article: Vatankhah, S., Renaut, R.A., Mickus, K., Liu, S. & Matende, K. (2022) A comparison of the joint and independent inversions for magnetic and gravity data over kimberlites in Botswana. *Geophysical Prospecting*, 70, 1602–1616. https://doi.org/10.1111/1365-2478.13265

13652478, 2022, 9, Downloaded from https://onlinelibrary.wiley.com/doi/10.1111/1365-2478.13265 by Arizona State University Acq & Analysis, Lib Continuations, Wiley Online Library on [19/10/2022]. See the Terms and Conditions (https://onlinelibrary.wiley.com/terms-and-conditions) on Wiley Online Library for rules of use; OA articles are governed by the applicable Creative Commons License